Statistical properties of the dense hydrogen plasma:
An *ab initio* molecular dynamics investigation

Jorge Kohanoff[1,2] and Jean-Pierre Hansen[2]

[1]*International Centre for Theoretical Physics, Strada Costiera 11, I-34014 Trieste, Italy*
[2]*Laboratoire de Physique, URA 1325 du CNRS, Ecole Normale Supérieure de Lyon, F-69364 Lyon Cedex 07, France*

The hydrogen plasma is studied in the very high density (atomic and metallic) regime by extensive *ab initio* molecular dynamics simulations. Protons are treated classically, and electrons in the Born-Oppenheimer framework, within the local density approximation to density functional theory. Densities and temperatures studied fall within the strong coupling regime of the protons. We address the question of the validity of linear screening, and we find it yields a reasonably good description up to $r_s \approx 0.5$, but already too crude for $r_s = 1$ (with $r_s = (3/4\pi\rho)^{1/3}$ the ion sphere radius). These values are typical of Jovian planets interiors. Finite-size and Brillouin zone sampling effects in metallic systems are studied and shown to be very delicate also in the fluid (liquid metal) phase. We analyze the low-temperature phase diagram and the melting transition. A remarkably fast decrease of the melting temperature with decreasing density is found, up to a point when it becomes comparable to the Fermi temperature of the protons. The possible vicinity of a triple point bcc-hcp(fcc)-liquid is discussed in the region of $r_s \approx 1.1$ and $T \approx 100 - 200$ K. The fluid phase is studied in detail for several temperatures. The structure of the fluid is found to be reminiscent of the underlying bcc (solid) phase. Proton-electron correlations show a weak temperature dependence, and proton-proton correlations exhibit a well-defined first coordination shell, thus characterizing fluid H in this regime as an atomic liquid. Diffusion coefficients are computed and compared to the values for the one-component plasma. Vibrational densities of states (VDOS) show a plasmon renormalization due to electron screening, and the presence of a plasmon-coupled single-particle mode up to very high temperatures. Collective modes are studied through dynamical structure factors. In close relationship with the VDOS, the simulations reveal the remarkable persistence of a weakly damped high-frequency ion-acoustic mode, even under conditions of strong electron screening. The possibility of using this observation as a diagnostic for the plasma phase transition to the fluid molecular phase at lower densities is discussed. [S1063-651X(96)01506-1]

PACS number(s): 52.25.Kn, 05.30.Fk, 64.70.Dv

I. INTRODUCTION AND STATE OF THE ART

The possibility of hydrogen metallization under high pressure was first discussed by Wigner and Huntington in the thirties [1]. This particular subject was included in the more general conjecture that any system becomes metallic if sufficient pressure is applied. Electrons, which are bound in the isolated atomic or molecular species, hybridize in a condensed phase to form extended states which gather in energy bands. When pressure is applied, the bands widen due to the enhancement of the overlap between neighboring atoms' orbitals, up to the point at which the energy gap between the valence and the conduction band vanishes, thus giving rise to metallic behavior. This enhancement of the overlap can also be viewed as the growing importance of the electronic kinetic energy relative to the ion-electron potential; the latter tends to bind electrons to the ions (also in the form of interatomic, intramolecular or intermolecular bonds). In the case of pure hydrogen, metallization was estimated to occur around 2.5 Mbars (1 Mbar = 100 GPa), i.e., at pressures that have become accessible to experiment in diamond anvil cells only very recently [2]. The absence of clear signs of metallic behavior up to 2.9 Mbar [3,4] certainly adds to the challenge, and stimulates the continuous improvement of experimental setups in the search for the *reluctant* metallization.

An additional difficulty in the description of this particular metal-insulator phase transition arises from the fact that at low pressures the low-temperature phase is not a monoatomic but a molecular solid, i.e., a hexagonal-close-packed (hcp) arrangement of H_2 molecules [2]. In this sense, H behaves more like a halogen than like an alkali metal [5]. Up to pressures of the order of 1 Mbar, experiment indicates that the hcp arrangement is preserved. At pressures of the order of 110 GPa, the low-pressure free-rotator phase of para-H_2 freezes into an orientationally ordered phase, whose nature is not yet fully understood. The observation of more than one vibron mode [6] precludes the hcp structure with all the molecules pointing along the c axis. However, other more complex hcp structures with tilted molecules (herringbonelike) are compatible with the experiment [2]. It is also possible that the orientational order is not complete, thus giving rise to a sequence of weak phase transitions until the perfectly ordered phase is reached.

An intriguing phase transition at 150 GPa, signalled by a discontinuity in the molecular vibron [7], has been ascribed either to a relative reorientation of the H_2 groups [8], to metallization arising from an electronic band-overlap mechanism without molecular reorientation [9], and to both occurring at the same time [10]. Density functional (DFT) calculations indicate that arrangements with complex molecular orientations (nonparallel) are energetically preferred in the high-pressure phase [8]. Another study [11] concentrated on

other classes of structures including cubic $Pa3$ and rutile, and also two molecular hcp structures with different relative orientations in the alternate planes, namely, $Pca2_1$ and $P2_1/c$. The hexagonal $Pca2_1$ was found to be the favorable one above the 150 GPa transition. Very recently, Tse and Klug performed *ab initio* simulated annealing calculations with 96 H atoms in the supercell, and found as a ground state an orthorombic structure, instead of hcp, composed of groups of three strongly interacting H_2 molecules [12]. All these candidates were found to be insulating, and the reason for this was claimed to be the opening of a hybridization gap at the Fermi level [13]. Diffusion Monte Carlo (DMC) calculations by Natoli, Martin, and Ceperley [14] have essentially confirmed results by Kaxiras, Broughton, and Hemley [8], also at the quantitative level for the angles between different molecular units. They considered neither Nagara's $Pca2_1$ nor Tse's orthorombic structure. This DMC calculation also finds an insulating behavior and, interestingly, zero-point-motion effects due to the protons appear to be quite structure independent. As a consequence, zero-point motion would turn out to be irrelevant as regards the 150 GPa transition, contrarily to the claims of Surh, Barbee, and Mailhiot [10].

Well-converged local density functional (LDA) calculations supplemented with the zero-point energy contribution taken from their frozen-phonon calculations [15], suggest that the molecular-hcp phase goes over directly to an atomic squeezed-hexagonal phase, by breaking the intramolecular bonds, at a pressure of 380 GPa. However, this calculation did not take into account nonhexagonal structures. Hence, also from the theoretical point of view, it is not clear up to now whether metallization happens already in the molecular phase, or whether it is a consequence of dissociation, thus occurring simultaneously with the molecular-atomic transition [3]. A rhombohedral structure was also postulated to supersede the squeezed-hexagonal phase at higher pressures (above 400 GPa) [16], while the transition to a body-centered-cubic (bcc) phase was located at around 1100 GPa [15].

In general, static methods suffer from the drawback of having to carry out the investigation by *guessing* different structures. In this respect, the molecular dynamics (MD) results by Tse and Klug seem to be the most reliable. However, there is still some doubt because it is not obvious that their 96-atom supercell with Γ-point sampling and fixed cell volume and shape calculation is a sufficiently good description. A recently proposed method that combines state-of-the-art electronic structure calculations with a variable cell shape MD simulation [17], thus avoiding every undesired bias, is currently being used to investigate the low-temperature phase of H as a function of pressure [18].

It is important to remark that, in general, energy differences between different structures are quite small, so that different levels of approximation often lead to different ground-state structures. In this respect, fully quantum-mechanical DMC calculations are very indicative. Ceperley and Alder [19] located the molecular-to-atomic phase transiton at a pressure of about 300 GPa, by studying only cubic structures. Further refinements of these DMC calculations have shown how dramatic the effect of improving the description can be [20]. Eventually, it appears that the atomic

ground-state structure in the vicinity of the molecular-atomic transition is the diamond structure, but the energy difference with respect to others is very small and, in particular, with respect to β-Sn and hexagonal diamond, it is well within the error bars. The diamond structure was considered as a candidate for the ground state in one of the previous DFT calculations, but found to be less favorable than a distorted hexagonal phase [15].

The monoatomic bcc structure is unequivocally identified as the ground state in the very high density limit. There, the electronic kinetic energy is largely dominant over the remaining contributions, such that the electrons behave essentially as free fermions; i.e., the electronic subsystem decouples from the protons and becomes a rigid, homogeneous electron gas, which acts only as a neutralizing background for the protons. This is well known as the one-component plasma (OCP) model, whose classical version was shown to crystallize into the bcc structure. This follows from a simple calculation of the Madelung energy, although the energy differences relative to other structures turn out to be rather small. In the classical OCP, which was thoroughly studied during the past two decades [21], the bcc structure turns out to be the stable one also at finite temperature and up to the melting point. The quantum version of the OCP at finite temperatures has not yet been studied in detail. A numerical study using the path integral Monte Carlo technique (PIMC) is currently under development [22].

At higher temperatures the protons begin to behave as classical particles. The degeneracy temperature for the protons can be estimated to be of the order of $T_d^p \approx 180$ K$/r_s^2$, (with r_s the dimensionless density parameter—see below) by comparing the mean interprotonic distance and the thermal de Broglie wavelength. The electron degeneracy temperature (T_d^e) lies well above (by a factor $m_p = 1836$) such that, at temperatures lower than $T_d^e \approx 326000$ K$/r_s^2 = 1$ hartree$/r_s^2$, electrons can be considered to follow the protons adiabatically, always staying in the ground state compatible with the current protonic configuration (Fermi temperatures are about twice these numbers, e.g., $T_F^p = 326$ K$/r_s^2$). This latter approximation allowed Hohl *et al.* [23] to examine the hot, dense *molecular* phase by means of *ab initio* molecular dynamics (AIMD) simulations, and also to make some progress regarding the low-temperature structure. The AIMD study of the *atomic* phase is the subject of this and of a previous publication [24]. The effect of excited electronic states in the same regime has very recently been explored by an AIMD scheme using Mermin's density functional [25], and the fully quantum PIMC method was applied to simulate the very high-temperature fluid phase [26], where the number of excited electronic states involved becomes too large to be treated efficiently with Mermin's functional. The low-temperature regime, where protons in turn become degenerate, requires different simulation techniques which are currently being developed [27].

High-temperature high-pressure measurements on hydrogen have been very recently reported in shock wave experiments [28]. Pressures between 1 and 2 Mbar and temperatures of some thousand K are now feasible and rather controllable, and further expansion of this range is in sight. In such experiments, Nellis *et al.* observed the metallization of fluid molecular hydrogen at $P = 1.4$ Mbar and

$T = 3000$ K, a temperature which is significantly lower than that predicted for the plasma phase transition by Chabrier *et al.* [29] on the basis of a multicomponent thermodynamic theory that employs an approximate equation of state. Although more accurate PIMC simulations have essentially confirmed the predictions of the theory, including the existence of a first order phase transition at high pressures and a somewhat lower value for the transition temeprature [30], the discrepancy with respect to shock wave experiments and AIMD results [31] still holds. The latter would rather indicate a continuous transition in which metallization and dissociation of H_2 molecules are closely related phenomena. A possible scenario would be the existence of two phase transitions: a continuous one, at relatively low temperatures, where molecular hydrogen already metallizes and begins to dissociate, and a discontinuous one at higher temperatures where a massive dissociation occurs with a concomitant jump in the electrical conductivity.

Hydrogen at finite temperatures and high densities consitutes, hence, a strongly coupled proton-electron plasma which is of great astrophysical interest since it is, in particular, the major constituent in Jovian planet interiors. Actually, the latter are basically H plasmas with a few percent admixture of He, and the statistical properties of the mixture (mixing-demixing transition) are of great importance to account for experimental observations and to establish models for the evolution of these planets [32]. Nevertheless, the answer to many relevant questions in astrophysics requires a full understanding of the statistical properties of the pure main constituents. Hydrogen is present in both atomic and molecular fluid phases. These are separated by a boundary located at some distance from the center of the planet. The characteristics of this boundary, e.g., precise location, width, etc. depend on the density and temperature profile, i.e., on the equation of state. The matter of dissociation and metallization is particularly relevant because the large magnetic field measured in Jupiter would include a non-negligible component generated in the outer molecular fluid phase, provided that temperature is above the metallization threshold. To quantify this effect the important quantities are the dissociated fraction and the electrical conductivity, which can be obtained from simulations in the molecular phase.

The hydrogen plasma is perhaps the most fundamental, simple many-body system, with *all* the interactions (proton-proton, proton-electron, and electron-electron) described exactly by the *bare* Coulomb potential. In spite of this, the phase diagram appears to be surprisingly rich. The purpose of this article is to present a detailed study of the very high-pressure physical properties and phase diagram of this simple and fascinating system. We are going to deal always with atomic phases, the molecular phases appearing at lower densities than those studied here. In Sec. II we briefly describe some details of the simulations, and we address some important technical issues such as the interplay between pseudopotentials and basis set expansions. Section III is devoted to the analysis of the validity of linear response theory in its ability to describe proton-proton interactions in terms of an effective pair potential of the screened Coulomb form. In Sec. IV we address a crucial problem that arises in the *ab initio* simulation of metallic systems, in particular liquid metals, i.e., size effects and Fermi surface sampling. In Sec. V

we enter directly into the properties of the hydrogen plasma by describing the solid phases and the melting at very high pressure. Section VI is concerned with the fluid phase, which we characterize as atomiclike. Diffusion and vibrational properties are presented in Sec. VII, while Sec. VIII is devoted to a thorough study of the collective dynamics, as an approach to the metal-insulator transition coming from the metallic side. The behavior of the longitudinal collective mode is studied as a function of density and temperature, and proposed as a probe for the metal-insulator transition at finite temeprature. Finally, we conclude in Sec. IX. In the remaining part of this Sec. I we define some useful parameters and ratios.

The plasma is made up of n electrons and as many ions (protons) per unit volume, such that the usual dimensionless density parameter is $r_s = a/a_B = (3/4\pi n)^{1/3}/a_B$, where a is the mean interionic distance (ion-sphere radius) and a_B is the bohr radius. Adopting atomic units throughout, the Fermi momentum is $k_F = (9/4\pi)^{1/3}/r_s$, and the Thomas-Fermi screening length is $k_{TF} = (12/\pi)^{1/3}/\sqrt{r_s}$. The dimensionless Coulomb coupling constant associated with the classical ions is $\Gamma = e^2/(a k_B T)$. Note that $k_B T = 1/(\Gamma r_s)$, and that the electron degeneracy parameter is $\theta = T/T_F = 2(4/9\pi)^{2/3} r_s/\Gamma$. Typical densities inside Jovian planets are between 1 and 10 g/cm^3 and temperatures are of the order of 100 to 10000 K, i.e., r_s ranging from 0.5 to 1.5, and $\Gamma \approx 20-200$ [21]. Note that within this range $\theta \approx 0.015 \ll 1$ and for the present calculations, whose aim is precisely to address some aspects of astrophysical plasmas, we can resort to the adiabatic approximation by assuming that the electrons are always in their instantaneous ground state for any given ionic configuration. Higher temperatures require the relaxation of this hypothesis.

II. TECHNICAL DETAILS OF THE SIMULATIONS

Our simulations were carried out using the standard Car-Parrinello (CP) AIMD scheme [33]. The ions were considered as classical pointlike particles, whereas the electrons were described by density functional theory (DFT) within the local density approximation (LDA) [34]. The electronic density was constructed via Kohn-Sham single-electron orbitals, expanded in a plane wave basis set up to a specified energy cutoff E_{cut} (see below). We have extensively studied a system consisting of 54 H atoms contained in a simple cubic simulation box under periodic boundary conditions (PBC), and we have also performed simulations for larger supercells, containing 128 and 162 H atoms, in order to analyze finite-size effects. The plane wave expansion was carried out around the Γ point of the supercell's Brillouin zone. Finite-size and Brillouin zone sampling effects will be analyzed later, in a forthcoming section.

We used the exchange-correlation functional deduced from the results of quantum Monte Carlo calculations on the uniform electron gas [36], and the bare Coulomb potential for the ion-electron interaction. The singularity of the ion-electron Coulomb attraction implies that there is never absolute convergence of the electronic quantities as the energy cutoff for plane waves is increased. In particular, the cusp condition is never satisfied, the density reaching the origin with zero slope. This is because the Fourier expansion of $1/r$ is also a long-range function $(4\pi/g^2)$, meaning that there
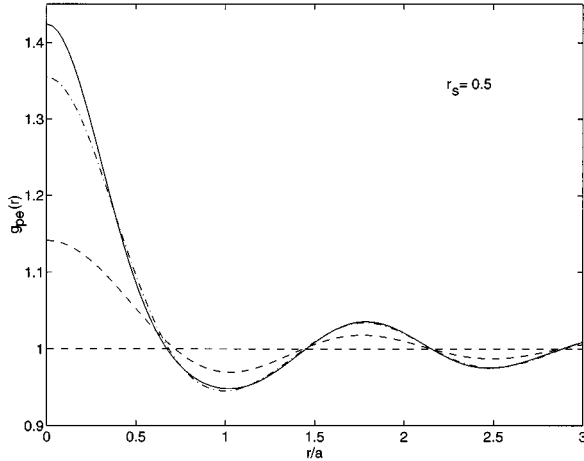
FIG. 1. Electron distribution around the proton site for H in the perfect bcc structure at $r_s = 0.5$, as a function of the plane wave energy cutoff. Dotted, dash-dotted, and solid curves correspond to cutoffs of 60, 230, and 420 Ry, respectively.

always exists a spatial scale small enough to require a representation involving large-g components. To satisfy the cusp condition, a different (localized) basis set is needed instead of plane waves, e.g., Slater-type orbitals [37]. A finite cutoff $g_{cut} = \sqrt{2E_{cut}(\text{Ry})}$ translates into the following effective potential:

$$v_{eff}(r) = \frac{1}{r}\left(1 - \frac{2}{\pi}\int_{g_{cut}}^{\infty} \frac{\sin(x)}{x} dx\right). \qquad (2.1)$$

This description is variational in the number of plane waves (i.e., in the energy cutoff) and, even if the energy never fully converges, other quantities, like the electronic distribution around the protons, are affected only in a tiny region around the nuclei, the remainder being essentially converged at a finite cutoff. This is shown in Fig. 1 for protons fixed at the ideal bcc lattice sites. The choice of the cutoff strongly depends on the average density: the lower r_s, the higher the cutoff. It is the number of plane waves which has to be kept approximately constant in order to achieve similar levels of convergence. In order to have the electronic density correctly described from less than one third of the nearest-neighbor ionic distance onward, we decided to vary the cutoff between 230 Ry for $r_s = 0.5$ and 60 Ry for $r_s = 1$ and 1.2. It can be seen in Fig. 1 ($r_s = 0.5$) that differences in the proton-electron correlation function become noticeable at distances smaller than $0.5a$, while the nearest-neighbor distance in the bcc lattice is $d_{nn} = 1.76a$. It should be pointed out that a cutoff of 60 Ry is sufficient to achieve convergence in the properties of the H_2 molecule, like the proton-proton distance (1.5 a.u. = 0.79 Å) and the vibrational frequency (4160 cm^{-1}). The difference with respect to the experimental quantities (0.74 Å and 4400 cm^{-1}) may be ascribed exclusively to the LDA.

Isothermal ionic dynamics (particularly in the fluid phase) was achieved by using a Nosé-Hoover thermostat. The time step for integration of the CP equations of motion was chosen typically between 0.25 and 1.5 a.u. (depending on the temperature and density), i.e., roughly 10^{-17} s, compared to the ionic plasma period $\tau_P \approx 155 \, r_s^{3/2}$ a.u.. In some cases another Nosé thermostat was necessary to keep the fictitious kinetic energy of the electronic degrees of freedom at low values. Most runs extended over 0.4 to 0.6 psec, which amounts to more than 50 plasma oscillations. Before this, we allowed for the thermal equilibration during an initial period of 0.2 psec in the solid phase, and 0.8 to 1.2 psec in the fluid phase. The densities $r_s = 0.5$, $r_s = 1$, and $r_s = 1.2$ were explored in detail for temperatures in the range 100 K $\leq T \leq 10\,000$ K, which correspond to the strong coupling regime ($\Gamma \geq 30$), and cover both fluid and solid phases of the ionic component. In particular, $r_s \approx 1$ and $T \approx 7000$ K are typical conditions inside Jovian planets [38]. The simulations at $r_s = 1.2$ were carried out only in the fluid phase because the stable solid no longer has the bcc symmetry, and thus it is not compatible with the choice of 54 H atoms in a simple cubic supercell.

III. VALIDITY OF LINEAR RESPONSE THEORY

In the very high density limit ($r_s \to 0$) the electrons are barely polarized by the ionic charge distribution, due to their rapidly increasing Fermi energy, and the hydrogen plasma practically reduces to two decoupled components: a classical ionic "one-component plasma" (OCP), and a degenerate, rigid electron "jellium." Both systems have been extensively studied by classical [21] and quantum [36] computer simulations. For finite, but small r_s ($r_s \ll 1$), the coupling between the two components may be treated perturbatively within linear screening theory [39]. However, due to the strength of the unscreened Coulomb interaction between protons and electrons, such a perturbative approach is expected to break down rapidly as r_s increases. In this section we investigate the high density limit and the validity of the description of the hydrogen plasma in terms of a linear response picture (LRT) for the electronic component.

To this end we compare the proton-electron pair correlation function taking into account the full LDA response:

$$g_{pe}(r) = -\frac{V}{N^2}\int d\mathbf{k}\langle\rho_i(\mathbf{k})\rho_e(-\mathbf{k})\rangle j_0(kr) \qquad (3.1)$$

and the one obtained by replacing the electronic charge density by its linear response expression in terms of the ionic charge density

$$\rho_e(\mathbf{k}) = \chi_e(k)\left(-\frac{4\pi}{k^2}\right)\rho_i(\mathbf{k}), \qquad (3.2)$$

where $\chi_e(k)$ is the static electron density response function. In Eq. (3.1), $j_0(x)$ denotes the $l = 0$ spherical Bessel function, $\rho_i(\mathbf{k})$ is a Fourier component of the microscopic ionic density, and $\rho_e(-\mathbf{k}) = \rho_e^*(\mathbf{k})$ is a Fourier component of the electronic density corresponding to the instantaneous ionic configuration $\{\mathbf{R}_I\}$. The latter represents, within the adiabatic approximation, a ground-state expectation value.

For the density response we adopt the random phase approximation (RPA) corrected by the long wavelength limit of the local field function $G(k)$ [21]
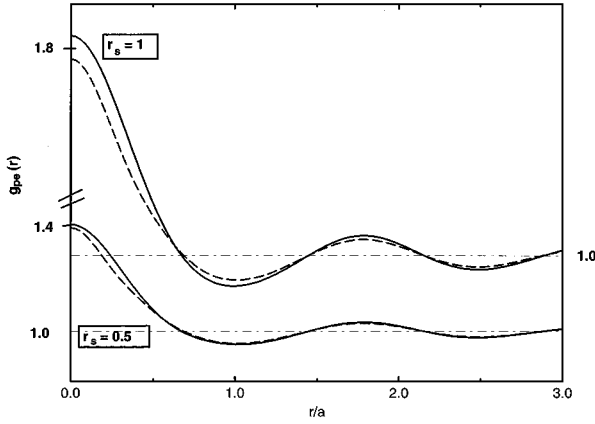
FIG. 2. Electron distribution around the proton site for H in the perfect bcc structure at $r_s = 0.5$ (lower curves) and $r_s = 1$ (upper curves), according to LDA (solid lines), and within linear response (dashed lines). Distances expressed in units of the ion-sphere radius $a = r_s a_B$.

$$\frac{4\pi}{k^2}\chi_e(k) = \frac{k_{TF}^2 l(k/k_F)}{k^2 + k_{TF}^2 l(k/k_F)[1 - G(k/k_F)]}, \quad (3.3)$$

with $l(x)$ the Lindhard function and k_{TF} the Thomas-Fermi wave number. For the local field correction we use the following expression, which is consistent with the LDA and Slater's local exchange:

$$G(k/k_F) = \left[\frac{1}{4} - \frac{\pi\lambda}{24}\left(r_s^3 \frac{d^2\epsilon_c(r_s)}{dr_s^2} - 2r_s^2 \frac{d\epsilon_c(r_s)}{dr_s}\right)\right]\frac{k^2}{k_F^2}, \quad (3.4)$$

where the correlation energy density $\epsilon_c(r_s)$ is that proposed by Perdew and Zunger [40], and $\lambda = (4/9\pi)^{1/3}$. At typical densities studied in this work the exchange contribution to $G(k/k_F)$ turns out to be largely dominant over correlation, and both of them represent a small correction relative to the RPA susceptibility. In fact, this is reasonable because the RPA (or Lindhard approximation) is known to be good in the high density limit.

The proton-electron distribution function reads accordingly

$$g_{pe}^{LR}(r) = \frac{V}{N^2}\int d\mathbf{k}\langle\rho_i(\mathbf{k})\rho_i(-\mathbf{k})\rangle j_0(kr)$$

$$\times\left(\frac{k_{TF}^2 l(k/k_F)}{k^2 + k_{TF}^2 l(k/k_F)[1 - G(k/k_F)]}\right). \quad (3.5)$$

In Fig. 2 we compare the proton-electron radial distribution functions in the ideal bcc structure as obtained from the LDA and from LRT, for $r_s = 0.5$ and $r_s = 1$. As expected, $g_{pe}(r)$ is considerably more structured at the lower density. The LDA and LRT distribution functions are very close at $r_s = 0.5$, but significant differences are clearly apparent at $r_s = 1$, reaching a region beyond the first ionic shell and signaling the breakdown of the linear screening regime. When the ions are at finite temperature the differences are significantly enhanced, particularly at short distances. Also the lo-
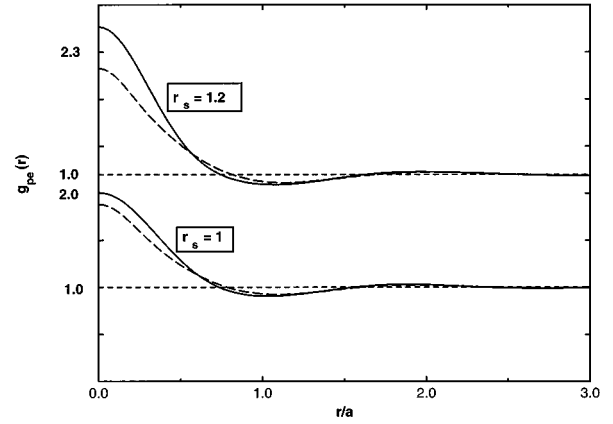

FIG. 3. Electron distribution around the proton site for H at T=2000 K according to LDA (solid line) and LRT (dashed line), for $r_s = 1$ (lower curves) and $r_s = 1.2$ (upper curves).

cation of the first minimum turns out to be shifted outwards by LRT in the fluid phase (unlike in the solid phase), thus indicating that the LRT description of the electronic charge distribution worsens for increasing temperature. This is shown in Fig. 3. The dashed curves have been obtained by averaging the adiabatic electronic charge distribution around the protons along the AIMD trajectory, assuming that the configurations generated in this way are also representative of the LRT. In fact, the magnitude of the differences observed in Fig. 3 suggests that the LRT trajectories will differ significantly from the LDA ones, implying that this averaged electronic distribution might be meaningless within LRT. In other words, the fully consistent LRT is likely to be worse than the results presented here.

Following a recently introduced procedure [41] we have fitted, for $r_s = 1$, an effective proton-proton pair potential to our set of AIMD configurations generated at several temperatures spanning both solid and fluid phases. In Fig. 4 we compare this potential to the one obtained within LRT, i.e., by Fourier transforming $v_{LRT}(k) = 4\pi[1 - \chi_e(k)]/k^2$, where $\chi_e(k)$ is given by expression (3.3). The nearest-neighbor distance in the bcc structure for $r_s = 1$ is 1.76 a.u., and the
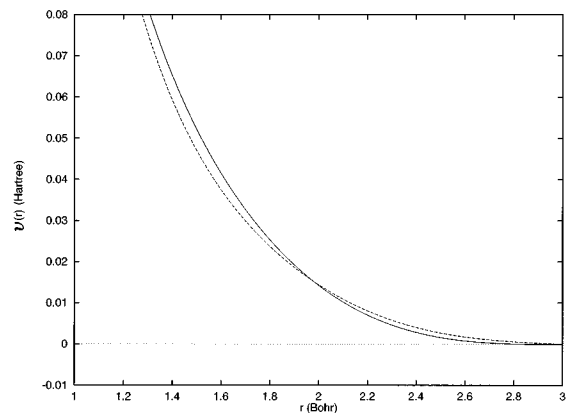

FIG. 4. Effective pair potentials for the proton-proton interaction at $r_s = 1$: v_{LDA} fitted to AIMD trajectories (solid line), and v_{LRT} obtained within the RPA with local field corrections (dashed line).

position of the first peak in the proton-proton radial distribution function decreases down to values of the order of 1.5 a.u. in the fluid phase and upon heating (see below). This means that nearest pairs of protons will spend most of the time at distances of this order. Looking carefully at Fig. 4 it can be seen that, at those distances, the two potentials differ by more than 10%, the LDA one being steeper. On the other side, the LRT pair potential appears to be more long ranged than the LDA one. This implies that the LDA pair potential has a characteristic screening length shorter than its LRT counterpart, i.e., screening is more efficient than linear at $r_s = 1$.

The departure from the linear screening regime, also in the form of many-body effects beyond the pair potential approach (e.g., three-body terms or embedding functions), becomes more pronounced as r_s is increased, leading to ground-state atomic phases other than bcc, fcc, or hcp (e.g., hexagonal and diamond) and, eventually, to recombination and to the different H_2 molecular phases. The reason for this early departure from the LRT regime has to be traced back to the unusual strength of the bare Coulomb interaction, arising from the absence of core electrons. In fact, other alkali metals can be reasonably well described by LRT at much lower electronic densities ($r_s > 3$) [42]. Interestingly, the range of validity deduced here for the LRT is much wider than expected in previous theoretical work based on perturbative expansions [39], where $r_s = 0.1$ was identified as the upper limit.

IV. SIZE EFFECTS AND FERMI SURFACE SAMPLING

In the solid phase, the combination of Γ point sampling and a finite system size is not expected to provide a very accurate description of the electronic component, because all the periodicities beyond the size of the supercell are not properly included. This is particularly important in metallic systems, where no point in the Brillouin zone can be taken as representative of the band structure of the bulk solid. The reason is that occupied states (contributing to the electronic density) and empty states (which do not contribute) coexist in the same band, corresponding to different k points. A particular choice (e.g., the Γ point and its refolded images) will sample the conduction band in some specific points, but the character of the Fermi surface could be misinterpreted if empty states are taken as if they were occupied and vice versa. For quasispherical Fermi surfaces this is unlikely to happen, but for transition metals or semimetals (like graphite) this effect is crucial, and a very fine sampling of the Brillouin zone is needed to obtain the right physics.

In the case of simple metals the effect of quantization of the electronic states in the simulation box is more important. The Brillouin zone of the unit cell is sampled with a finite number of points, which arise from the refolding of the Γ point of the supercell. These points reflect the symmetries of the system in the sense that, if the Γ point refolds onto some point $\mathbf{k}_0$, then all the points in the star of $\mathbf{k}_0$ must arise from some other refolding of Γ. Otherwise, the symmetry is broken and spurious forces appear that drive the system away from the symmetric ground state. Depending on the case at hand, the distortion can be rather large, especially if the symmetry of the supercell is very different from that of the unit

cell. If the correct symmetry is used for the supercell then, since all the points in the star are equivalent, the eigenvalues associated with them are degenerate, thus giving rise to the formation of electronic shells. If a better sampling of the Brillouin zone is performed, or the size of the system is increased, new shells appear that eventually give rise to a continuous energy band. But for finite systems and restriction to the Γ point, the electronic density of states consists of a set of discrete peaks (the shells). A problem arises with the highest occupied shell because in finite-size metallic systems it is partially occupied, unless a very fortuitous situation occurs. The immediate consequence is that it is not possible to fullfil the symmetry requirements by occupying all the points in the star with an *integer* number of electrons. Then, unless *fractional* occupation is introduced, the symmetry is broken even when the symmetry of the unit cell is mantained for the supercell. This is analogous to the Jahn-Teller effect in molecular systems, where a lower-energy state can be obtained by reducing the symmetry and breaking the electronic degeneracy. However in the present case this effect is unphysical.

In a fluid phase these effects are normally expected to become less important because of the breakdown of the discrete translational invariance, as reflected in the very existence of a finite Brillouin zone via Bloch's theorem. The unit cell becomes of infinite size and the Brillouin zone reduces to a single point, i.e., the Γ point. However, for practical reasons, computer simulations are bound to represent the infinite (fluid) system with a limited number of particles (typically of the order of some hundreds in *ab initio* calculations), while repeating periodically the supercell (via PBC). In fact, this introduces a spurious Brillouin zone, which is associated with periodicities that are absent in the infinite fluid. The properties of the fluid are assumed to be recovered from the finite sample in terms of the PBC combined with statistical averages, which in the case of our AIMD simulations are computed as time averages.

This is a reasonable justification for a purely classical system and also for liquid semiconductors but, for metallic systems, as soon as electronic states are introduced, the quantization of these states in the (unphysical) simulation box acquires a crucial role. The problem of partial occupation of the star persists in the fluid, in the sense that spurious forces appear that modify in a nontrivial way the structural and dynamical properties of the system.

A qualitative picture of the consequences of these observations can be obtained by comparing the proton-proton radial distribution function for systems of different sizes. A system of 54 H atoms (of valence charge equal to 1) is really a fortuitous case of compatibility of a closed electronic shell (the whole star is fully occupied) with a bcc atomic arrangement in a simple cubic supercell. In the case of 128 H atoms only 57 states are doubly occupied, and the next shell of 24 degenerate states has to accomodate 14 electrons (i.e., only 30% of the shell). On the contrary, 162 H atoms is not compatible with a bcc arrangement in a simple cubic supercell, but it closes the former electronic shell thus amounting to 81 doubly occupied states. Therefore, in the fluid phase it should behave essentially as the 54-atom supercell but better converged in system size (or k points). In Fig. 5(a) we show the curves corresponding to these three different system sizes at $r_s = 1$ and $T = 1000$ K. In fact, up to the boundary of the
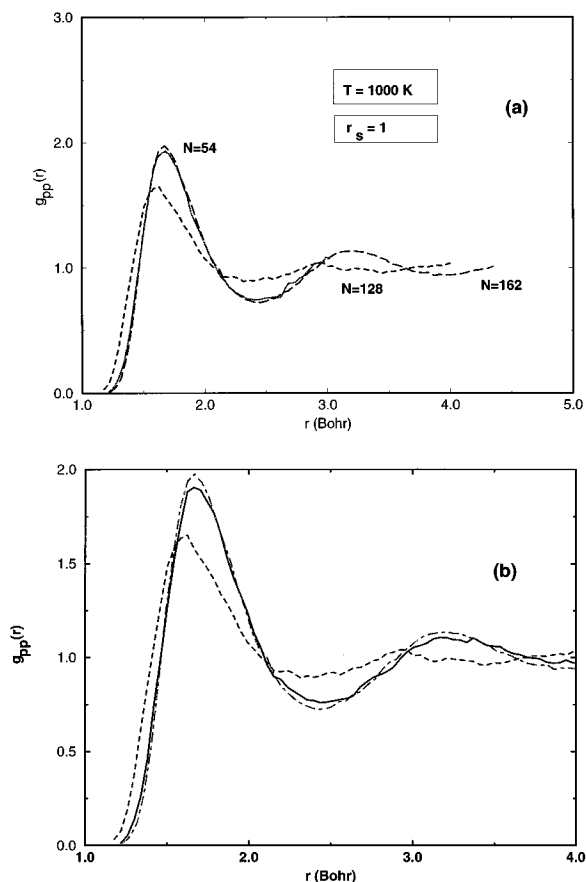
FIG. 5. Proton-proton pair distribution function at $T=1000$ K and $r_s=1$ for different system sizes: (a) 54 atoms (solid line), 128 atoms (dashed line), and 162 atoms (dotted line); (b) 128 atoms considering explicitly the whole open shell (81 states), where the lowest 64 are *initially* occupied (solid line), 128 atoms considering explicitly only the 64 lowest occupied states (dashed line), and 162 atoms (dot-dashed line).

54-atom cell ($r=3$ a.u.) there is hardly any relevant difference between the $g_{pp}(r)$ corresponding to 54- and 162-atom supercells. The same kind of picture holds also at higher temperatures, meaning that, as regards static thermodynamic properties, 54 H atoms already give a very reasonable picture.

Very different is the situation with open-shell systems like the 128 H atoms one [short-dashed line in Fig. 5(a)]. It is clear that this $g_{pp}(r)$ has little to do with those of 54 and 162 atoms. The first peak is significantly lower and broader, and also its position is shifted downwards. The first valley is much shallower and, in practice, the pair distribution becomes structureless beyond it, while with 162 atoms the atomic-shell structure is still visible at least up to the second valley. The 128-atom distribution resembles, in fact, the one that would have been obtained with closed shells at a higher temperature value.

The correct way to account for open-shell structures at finite temperature is to doubly occupy the lowest-lying electronic states at every time step of the AIMD simulation, while keeping empty the rest of that shell. The curves in Fig. 5(a) have been obtained by applying the standard procedure of considering explicitly, in the description of the electronic
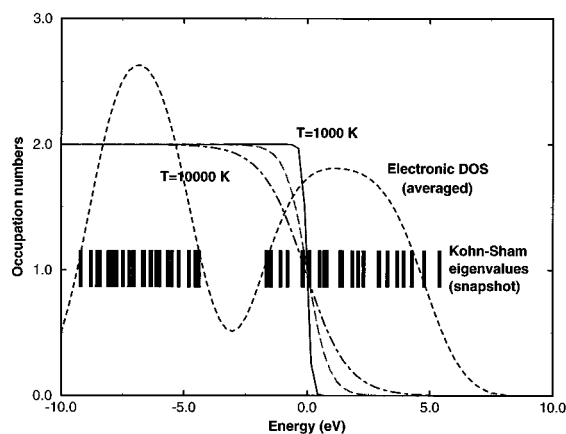
FIG. 6. Fermi-Dirac distribution function for $T=1000$ K (solid line), $T=5000$ K (long-dashed line), and $T=10000$ K (dot-dashed line). The electronic density of states associated with the last two occupied shells is also shown (short-dashed line), as well as a single shot of the Kohn-Sham eigenvalues during an AIMD simulation at $T=1000$ K (vertical bars). The EDOS is broadened with a Gaussian window 1 eV wide.

component, a number of electronic states equal to one half of the number of electrons, i.e., including those strictly necessary. The justification for this approach is that typical temperatures are much lower than the Fermi temperature. Atomic motion leads to a degeneracy lifting of the order of a few percent of an eV, implying that the distance between electronic states is usually much larger than the width of the Fermi-Dirac distribution; this latter is of the order of $k_B T$, i.e., about 0.1 eV at $T=1000$ K. This leads to a symmetry breaking in the sampling of the Fermi surface, which is expected to be recovered in terms of statistical averaging. However, following the approach above, in practical simulation times we have not noticed a convergence to the closed-shell picture. In Fig. 6 we show the Fermi-Dirac distribution function for three different temperatures, namely 1000 K, 5000 K, and 10 000 K, compared to the electronic density of states averaged along an AIMD run at $T=1000$ K, and to a snapshot of the instantaneous Kohn-Sham eigenvalues. It is clear that the occupation numbers fall from 2 to 0 in an energy scale narrower than the thermal splitting of the eigenvalues.

The drawback of this kind of approach is that for open shells the ordering of the states within the highest (partially) occupied shell changes continuously during the MD evolution and, in particular, occupied states become empty and vice versa. The standard CP approach is not able to take into account this phenomenon, and this is one reason for the well-known failure in metallic systems, reflected in the energy transfer between electronic and ionic degrees of freedom (cooling the ions and heating the electronic orbitals). The double Nosé thermostat proposed by Blöchl and Parrinello [43] helps in fixing the temperature of each of the components, but still does not take into account level crossing effects. To our knowledge, there are three methods capable of solving this problem: one is to abandon the CP Lagrangian strategy in favor of a self-consistent minimization at each time step [44], a second one is to abandon the description of the electronic component in terms of single-particle orbitals to work directly with the electronic density which is, by defi-

nition, constructed with the lowest occupied states [25], and finally a third one consisting of a rigorous Lagrangian formulation which incorporates the occupation numbers (actually the conjugate variables, i.e., the Kohn-Sham eigenvalues) as dynamical variables [45]. However, this latter procedure exhibits the odd feature that the fictitious kinetic energy of the electronic orbitals still increases at the expense of the ionic component, due to the appearance of low-energy excitations introduced by the dynamics of the eigenvalues.

An approximate solution can still be found within the Lagrangian approach by evolving explicitly the whole open shell, but initially occupying — with an integer number of electrons — only the lowest states of the this shell. This will approximately take into account level crossing in terms of mixing of states within the shell, during the time evolution. The very same mechanism that leads to energy transfer between ions and electronic orbitals, i.e., the vanishing energy gap [46], is responsible for mixing occupied and empty orbitals, thus allowing for initially empty states (if explicitly included) to become occupied and vice versa. Statistical averaging completes the task by generating a more uniform sampling of the Fermi surface. Figure 5(b) shows how the results obtained with 128 H atoms can reproduce approximately those obtained with 54 and 162 H atoms. It has to be pointed out that this procedure, although not rigorously justified, has the nice feature that the fictitious kinetic energy of the electronic orbitals is practically constant, behaving exactly as in systems with a gap, i.e., there is no energy exchange between ionic and electronic degrees of freedom.

V. LOW-TEMPERATURE PHASE: STRUCTURE AND MELTING

In the OCP ($r_s \rightarrow 0$) limit the ionic bcc lattice is known to be the stable crystalline structure up to melting (which occurs at $\Gamma \approx 180$ [21]). We have studied the stability of the bcc structure at low temperatures and finite r_s by performing canonical MD simulations; initial conditions were constructed by giving the ions a small random displacement (about 3% of the nearest-neighbor distance d_{nn}) from their alleged equilibrium positions (the bcc lattice sites). The bcc structure was found to be dynamically stable against such displacements at least up to $r_s = 0.5$. At $r_s = 1$ the bcc structure was found to be unstable for $T < 100$ K, where a close-packed structure appears to be favored. This is consistent with a description in terms of LRT. In fact, at high densities the effective LRT potential behaves essentially like a Yukawa potential

$$v_{SC}(r) = \frac{1}{r}\exp(-rk_{TF}), \qquad (5.1)$$

while Friedel oscillations are practically negligible. The phase diagram of a classical system of particles interacting via the above Yukawa potential (5.1) has been extensively studied by computer simulations and lattice dynamics [47]. These calculations point to a bcc-fcc phase transition when the density-dependent screening wave number increases, i.e., when the effective interaction becomes of shorter range. At $T = 0$ the bcc structure is found to be stable up to $r_s \approx 0.6$, beyond which the fcc phase becomes the stable structure.

The r_s at coexistence shifts to higher values at finite temperatures, such that the system goes through a structural fcc-bcc phase transition as the temperature increases along an isochore.

The situation here is reminiscent of the behavior of alkali metals. Na exhibits an hcp ground state, while Li goes from bcc to fcc and eventually to hcp at very low T. The heavier alkalis K, Rb, and Cs undergo a structural transition to fcc upon cooling below $T \approx 5$ K. In all these cases the entropic contribution of the bcc structure, arising from the valley in the phonon dispersion along the (110) direction, wins over at finite temperature and stabilizes this phase. This is exactly what we observe in our simulations for H, where at $r_s = 1$ the bcc structure appears to be stable for $T > 100$ K.

Still, the finite energy cutoff, finite system size, and coarse Brillouin zone sampling may have a large influence on the stability of the ground-state structure. The study of this part of the phase diagram deserves special attention because also zero-point motion effects on the protons have been shown to influence the stability of different structures at $T = 0$ [20]. Disregarding the problem of zero-point energy (ZPE), and only as a check of the present calculations (which do not include ZPE), we have performed total energy full potential-linear muffin tin orbitals (FP-LMTO) calculations for solid, monoatomic H in the bcc, fcc, and hcp structures, at $r_s = 0.5$ and $r_s = 1$. The energy differences turned out to be very small, but at $r_s = 1$ the fcc and hcp structures are significantly lower in energy than the bcc. Moreover, the energy differences are enhanced if a coarse sampling of the Brillouin zone is performed. These calculations also identify the hcp structure as the lowest energy one, but the difference with respect to the fcc is within the accuracy of the calculations. The reason for this can be found in Fig. 4. The differences between fcc and hcp structures begin only at the level of third nearest neighbors, a region where the effective potential shows only negligibly small Friedel oscillations.

Between $r_s = 1$ and 1.2 a phase transition occurs that takes the system from hcp to a simple-hexagonal phase with a compressed c/a ratio (squeezed hexagonal). This is compatible with static total energy calculations by Barbee *et al.* [15], and it is an additional confirmation of the breakdown of LRT, because pair potentials of the LRT type are not able to stabilize anisotropic structures like the simple hexagonal. A more detailed study of the low-temperature atomic phases of hydrogen is currently under way [18].

Next, the melting of the ionic crystal was investigated by gradually increasing the temperature and monitoring the time-dependent mean square displacement of the ions $\langle|\Delta\mathbf{r}(t)|^2\rangle = \langle|\mathbf{r}(t) - \mathbf{r}(0)|^2\rangle$. In the crystalline phase, $\langle|\Delta\mathbf{r}(t)|^2\rangle$ goes over to $2\langle|\delta\mathbf{r}|^2\rangle$ for sufficiently long times, where $\langle|\delta\mathbf{r}|^2\rangle = \langle|\mathbf{r} - \mathbf{R}|^2\rangle$ denotes the static mean square displacement ($\mathbf{R}$ are the equilibrium positions of the ions). In the fluid phase diffusion sets in, so that $\langle|\Delta\mathbf{r}(t)|^2\rangle = 6Dt$ at long times, with D the ionic diffusion constant. At $r_s = 0.5$ diffusion was found to set in at $\Gamma \approx 230$, which may be identified with the limit of mechanical stability of the (overheated) metastable crystal. The thermodynamic transition occurs at lower temperature (higher Γ); its location may be estimated by assuming that the Lindemann ratio $L = (\langle|\delta\mathbf{r}|^2\rangle)^{1/2}/d$ at melting is the same as for the OCP, i.e., $L \approx 0.15$ [35]. This leads to $\Gamma_m(r_s = 0.5) \approx 290$ compared to
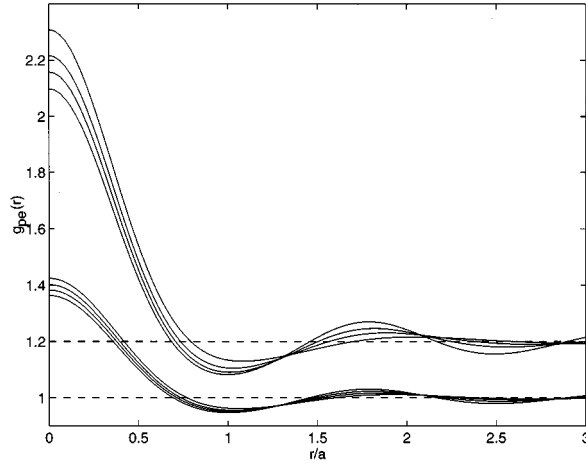
FIG. 7. Proton-electron pair correlation function at finite temperature (solid and fluid phases) at $r_s = 0.5$ and $T = 1000$, 2500, 5000, and 10 000 K (lower curves), and at $r_s = 1$ and $T = 200$, 500, 1900, and 7300 K (upper curves). The lower curve of each set corresponds to the lower temperature.

$\Gamma_m(r_s = 0) \approx 180$, indicating a strong influence of electron screening on the melting transition. This confirms recent predictions based on free energy comparisons, obtained by means of an approximate density functional theory [35].

We have also studied the melting transition at $r_s = 1$ using the same procedure; the melting temperature drops sharply from $T_m(r_s = 0.5) \approx 2200$ K to $T_m(r_s = 1) \approx 350$ K [$\Gamma_m(r_s = 1) \approx 930$]. This indicates the possible proximity of a triple point bcc-hcp(fcc)-liquid, analogous to that found for Yukawa potentials. However, the nonlinearity of the screening at these values of r_s is likely to bring the triple point from $r_s = 3$ [47] to $r_s \approx 1.1$. Moreover, the hcp structure goes over to a simple hexagonal one at r_s somewhere between 1 and 1.2, and this has to be a consequence of the appearance of anisotropic forces, beyond the level of pair-wise additivity. The very low value of the melting temperature might also be related to the appearance of these forces. Interestingly, at $r_s = 1$ the Fermi temperature of the ionic component is $T_F^p = 326$ K, a value close to the melting point (350 K). Therefore, the influence of quantum effects for the protons on the melting transition cannot be ignored, and will probably also play an important role in the above structural phase transition. In particular, they might destabilize the hexagonal phase in favor of some more isotropic configuration which has a higher energy within a framework of classical protons.

VI. THE FLUID PHASE: AN ATOMICLIKE PLASMA

Turning to the fluid phase, a quantitative measure of ion-electron correlations is provided by the sphericalized average of the ion-electron pair correlation function $g_{pe}(r)$, as computed from Eq. (3.1). The effect of temperature on $g_{pe}(r)$ is illustrated in Fig. 7, for $r_s = 0.5$ and $r_s = 1$. The distribution function is seen to be remarkably insensitive to T over the whole range of temperatures, covering the solid and fluid phases, as already noticed at lower Γ (higher T) by Dharma-Wardana and Perrot in the framework of an approximate static DFT hypernetted chain calculation [48]. The observed

weak temperature dependence implies that the main effect of ionic thermal motion (electrons are always at $T = 0$), is to enhance the localization of the electronic charge close to the protons.

This behavior is to be contrasted with the predictions of higher-level theories that go beyond the Born-Oppenheimer approximation by including excited electronic states. Both, fully quantum PIMC [49] and Mermin functional [50] simulations imply that the ion-electron correlations become weaker as temperature increases. This is to be intuitively expected, but for temperatures much higher than the ones studied here. Excited electronic states are much more insensitive to ionic polarization effects, because they correspond to larger kinetic energies. In this way, for temperatures larger than a threshold value that can be estimated around $\theta = 0.1$, i.e., $T \approx 60000$ K for $r_s = 1$, the above localization effect due to ionic disorder starts to be compensated by the effect of electronic excitations, so that eventually the opposite trend will take over.

The ion-electron pair correlation functions for *all* temperatures are seen to intersect at a well-defined (reduced) distance from the proton site, irrespective of thermal ionic disorder and almost independently of density. We locate this value at $r^* \approx 1.3a$, and notice that the ratio $r^*/d_{nn} \approx 0.73$ is related to the ratio of the location of the nodes corresponding to the first two spherical Bessel functions [$j_0(x)$ and $j_1(x)$]. In fact, the electronic problem can be modeled, in a very crude approximation, as that of a particle in a spherical well; the corresponding radial solutions are precisely the spherical Bessel functions. Temperature effects can be mimicked by increasing the relative population of excited states with respect to $j_0(x)$. However, the location of the node of $j_1(x)$ (the leading excitation) relative to $j_0(x)$ (the ground state) does not depend on temperature. Since the location of the nodes is defined in units of the radius of the well, and this is identified with d_{nn}, which is proportional to r_s, the crossing should not depend significantly on density. The first maximum of $g_{pe}(r)$ is clearly associated with the location of the first coordination shell [the first maximum in $g_{pp}(r)$ — see below], which is quite natural since the electronic density peaks at the proton sites. It is interesting to notice that differences in the electronic screening properties between $r_s = 1$ and $r_s = 1.2$ are significant only in the vicinity of the protons, up to $r \approx 0.5a$.

The proton-proton pair correlation function for $r_s = 1$ is illustrated in Fig. 8(a), as a function of temperature. It can be observed that the first peak remains clamped at the nearest-neighbor distance ($d_{nn} = 1.76$) for temperatures below the mechanical stability limit [$T_s(r_s = 1) \approx 500$ K], while in the fluid phase it shifts continuously to shorter distances. The same plot shows that the location of the first minimum is quite insensitive to temperature. This, together with the fact that equivalent results are found at $r_s = 0.5$, defines quite univocally a first coordination shell of radius $r_{fcs} \approx 2.4a$ (with a the ion-sphere radius). The integrated number of particles is shown in Fig. 8(b) as a function of temperature. The main result is that the first coordination shell contains 14 atoms on average, implying that the short-range structure of the liquid is quite reminiscent of that of the solid, since the first coordination shell of the bcc structure (containing first and second nearest neighbors) also contains 14 atoms. Simulations performed with 162 H atoms show that this is a genu-
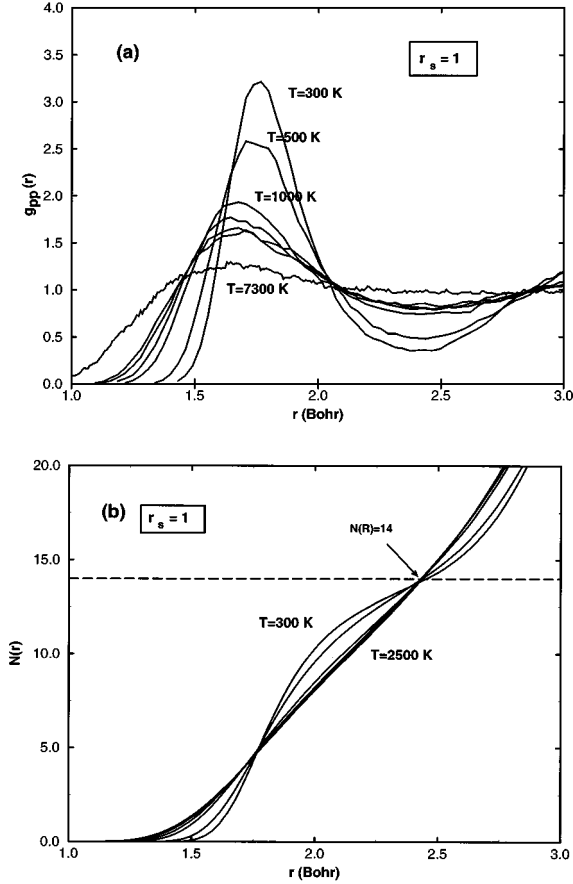
FIG. 8. (a) Proton-proton pair distribution function at $r_s = 1$ and $T = 300$, 500, 1000, 1500, 2000, 2500, and 7300 K. (b) Integral of the above distribution function for the same temperatures. The function $N(r)$ indicates how many protons are contained in a sphere of radius r, on average.

ine feature and not an artifact of the small system size. A second coordination shell is also well defined in the fluid phase provided that the temperature is low enough, i.e., $T < 1500$ K ($\Gamma > 200$), as can be observed in Fig. 9. How-
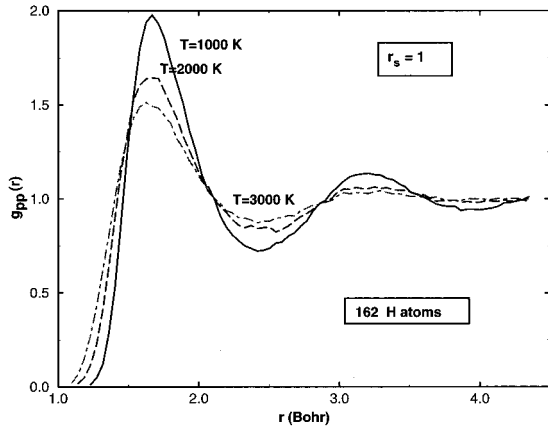
FIG. 9. Proton-proton pair distribution function at $r_s = 1$ for a 162 H atom sample, as a function of temperature: $T = 1000$ K (solid line), $T = 2000$ K (dashed line), and $T = 3000$ K (dot-dashed line).

TABLE I. Reduced (dimensionless) diffusion coefficient as a function of the plasma coupling parameter Γ. The error in the determination of the diffusion coefficients is $\Delta D^* = 0.001$.

r_s	Γ	D^*	T (K)
0.5	65	0.0122	10 000
0.5	90	0.0090	7500
0.5	130	0.0052	5000
0.5	210	0.0025	3100
1.0	108	0.0163	3000
1.0	130	0.0119	2500
1.0	163	0.0096	2000
1.0	217	0.0066	1500
1.0	326	0.0034	1000
1.2	136	0.0173	2000
1.2	181	0.0114	1500
1.2	217	0.0072	1000
1.2	272	0.0056	800

ever, the fluid becomes structureless beyond the first coordination shell at temperatures of the order of 5000 K (at $r_s = 1$). Summarizing, the fluid phase of the H plasma at moderately high temperatures and very high densities (typical of the inner H shell of Jovian planets) behaves like an atomic liquid with a well-defined first coordination shell.

The influence of electron screening is also apparent when comparing the ion-ion and charge-charge static structure factors $S_{ii}(k)$ and $S_{ZZ}(k)$. While at $r_s = 0.5$, the two are nearly indistinguishable, the amplitudes of their main peaks differ significantly for $r_s = 1$ (by roughly 9%), and $r_s = 1.2$ (12%). The strong polarization of the electronic component leads to a damping of the local charge fluctuations, and hence to a reduction of $S_{ZZ}(k)$. Due to the discrete sampling of the electronic density in reciprocal space, the curves are noisy and will not be reproduced here. Again, the presence of a well-defined first peak and valley in $S(k)$ is an indication that the fluid is well structured in this region of the parameter space.

VII. DIFFUSION COEFFICIENTS AND VIBRATIONAL PROPERTIES

Our AIMD simulations give direct access to the ionic dynamics by analyzing the time evolution of atomic coordinates and velocities. Diffusion coefficients have been calculated using the asymptotic relation $\langle |\Delta \mathbf{r}(t)|^2 \rangle = 6Dt$; i.e., by measuring the slope of the mean square displacement of the atoms as a function of time. Our results are displayed in Table I for $r_s = 0.5$, $r_s = 1$, and $r_s = 1.2$, in reduced plasma units $D^* = D/a^2 \omega_{\mathrm{pl}}$, where $\omega_{\mathrm{pl}}(r_s) = (3/M_I)^{1/2} r_s^{-3/2}$ is the bare ionic plasma frequency. The results are shown in a log-log plot in Fig. 10. The relationship between D^* and $\Gamma = 1/(r_s T)$ follows quite accurately a power law of the type $D^* = D_o \Gamma^\alpha$. We have fitted our data to such an expression, obtaining for $r_s = 1$ the following values: $D_o = (10.4 \pm 1.4)$ and $\alpha = (-1.38 \pm 0.07)$, and for $r_s = 0.5$ the values: $D_o = (4.0 \pm 1.5)$ and $\alpha = (-1.37 \pm 0.09)$.

It is interesting to note that the diffusion coefficient follows the same relationship as in the OCP model. The OCP
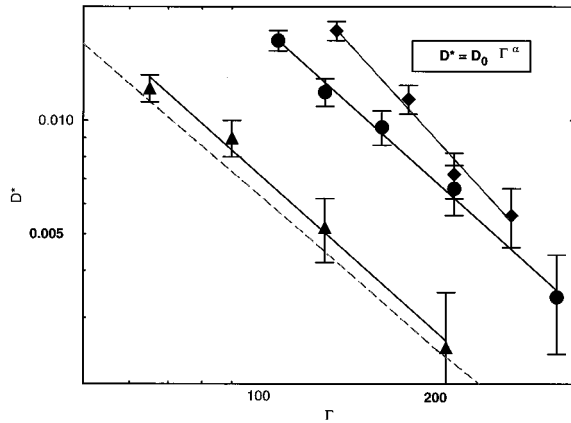
FIG. 10. Reduced diffusion coefficient at $r_s = 0.5$ (triangles), $r_s = 1$ (circles), and $r_s = 1.2$ (diamonds) in a log-log plot. Solid lines are the results of a linear regression fit on the logarithms. The dashed line is the OCP result.

FIG. 11. Velocity autocorrelation function at $r_s = 1$ for $T = 300$ K (dotted line), $T = 1000$ K (dashed line), $T = 2000$ K (dot-dashed line), and $T = 3000$ K (solid line). The abscissa (time) is expressed in units of the plasma frequency ω_{pl}.

values for the parameters, fitted to classical MD simulations [51] are $D_o = 2.95$ and $\alpha = -1.33$. The value of the exponent seems to be unaffected by electronic screening, at least within the accuracy of our calculations. The prefactor, however, is clearly enhanced from its OCP value, and this can be readily understood in terms of the response of the electronic component to the motion of the protons. A rigid uniform electronic background (as in the OCP) does not have any influence on the dynamics of the protons. A polarizable background weakens the proton-proton interaction thus increasing the mobility of the ions. In fact, the results obtained at $r_s = 0.5$ are quite close to the OCP values, represented by the dashed line in Fig. 10. The difference becomes much larger at $r_s = 1$, where D^* differs from its OCP values by a factor of 3; this contrasts with the Thomas-Fermi MD results of Zérah, Clérouin, and Pollock [52], who observed a much milder effect (a factor 1.4 at $\Gamma = 50$ and $r_s = 1$). Therefore, the diffusion coefficient appears to be very sensitive to the treatment of electron screening. The case of $r_s = 1.2$ is slightly different, because the exponent appears to be larger than the OCP value. However, it can be seen that the error bars are also compatible with an OCP-like power law, represented by a line parallel to that of the other densities.

The diffusion coefficient is also related to the ion velocity autocorrelation function (VACF), which, in the OCP limit, exhibits a striking oscillatory behavior due to a strong coupling of the single-particle motion to the collective ionic plasma oscillations [51]. Such oscillations were recently shown to persist at finite r_s, by MD simulations using the approximate Thomas-Fermi kinetic energy functional instead of the Kohn-Sham version [52]. The present *ab initio* calculations qualitatively confirm this behavior. In Fig. 11 we present the VACF for a typical simulation in the solid phase ($T = 300$ K) and then for three different temperatures in the fluid phase. The latter were computed in the supercell containing 162 atoms. Finite size effects are not very significant as regards the general features of the VACF. However, a small frequency shift is observed, and decorrelation happens faster in the larger sample. It is interesting to note that the fastest oscillation, i.e., the one associated with the ion plasma
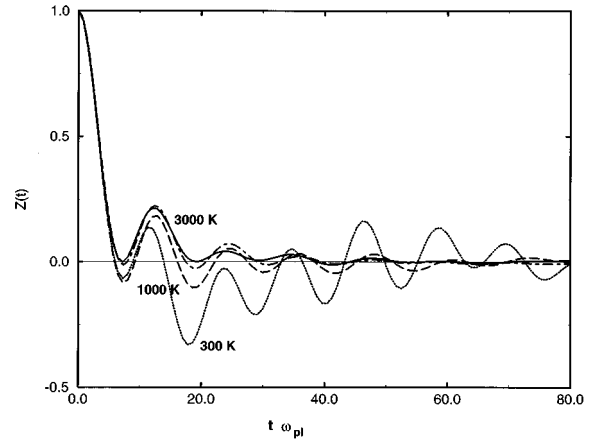
oscillations, is essentially temperature independent.

The power spectra of the ionic VACF are plotted in Fig. 12 for $r_s = 1$, at several temperatures. The spectra exhibit a high-frequency peak (or shoulder at the highest temperature) at a frequency which amounts to 55% of the bare ion plasma frequency (ω_{pl}). The power spectra for $r_s = 0.5$ are similar, with the difference that the high-frequency peak occurs now at a value which is 70% of the bare plasma frequency [24]. As expected, electron screening shifts the vibrational spectra to lower frequencies. Temperature, however, does not affect the position of the high-frequency peak, which remains the only well-defined feature at high temperatures, while the rest of the spectrum merges into a structureless continuum. These spectra were obtained from 54 H atom simulations. The 162 H atom sample yields a frequency 5% lower than the 54 H atom one.
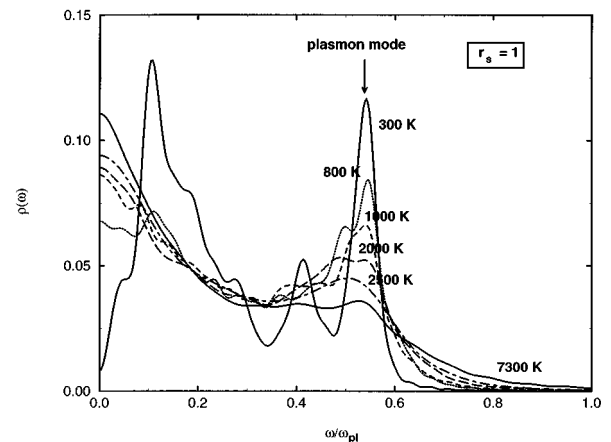

FIG. 12. Power spectra of the velocity autocorrelation function at $r_s = 1$, obtained by FT the velocity autocorrelation function. The curve at $T = 300$ K (solid line) corresponds to the solid phase, while the remaining curves correspond to $T = 800$ K (dotted), 1000 K (short-dashed), 2000 K (long-dashed), 2500 K (dot-dashed) and 7300 K (solid). These are all in the fluid phase. Frequencies are in units of the ionic plasma frequency ω_{pl}. Curves are normalized to integrate to the number of ionic degrees of freedom.
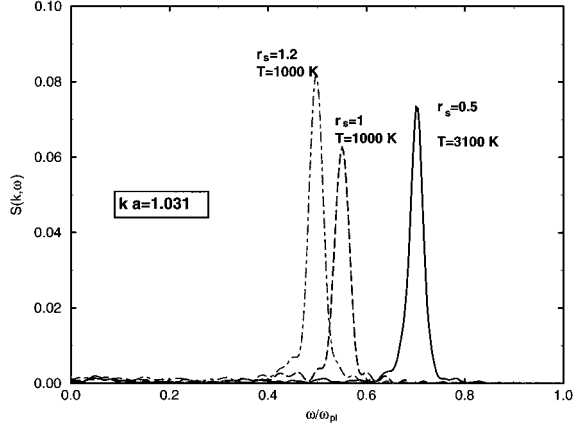
FIG. 13. Charge-charge dynamical structure factor at the smallest available wave vector, $ka = 1.031$, for three values of r_s.

VIII. COLLECTIVE MODES: A SIGNATURE OF THE METAL-INSULATOR TRANSITION

The oscillations in the VACF point to a long-lived longitudinal collective mode, related to the ionic plasmon mode of the OCP [51]. We have computed the charge autocorrelation function

$$F_{ZZ}(\mathbf{k},t) = \frac{1}{N}\langle \rho_Z(\mathbf{k},t)\rho_Z(-\mathbf{k},0)\rangle, \qquad (8.1)$$

where the Fourier components of the microscopic charge density are

$$\rho_Z(\mathbf{k},t) = \rho_i(\mathbf{k},t) - \rho_e(\mathbf{k},t), \qquad (8.2)$$

with ρ_i and ρ_e the AIMD-generated time-dependent densities. In keeping with the Born-Oppenheimer approximation, $\rho_e(\mathbf{k},t)$ is a Fourier component of the expectation value of the electronic density for the instantaneous ion configuration. In practice, we computed the average of $F_{ZZ}(\mathbf{k},t)$ over the shell of equal-modulus $\mathbf{k}$-vectors

$$F_{ZZ}(k,t) = \sum_{|\mathbf{k}|=k} F_{ZZ}(\mathbf{k},t). \qquad (8.3)$$

From this, we computed the dynamical structure factor $S_{ZZ}(k,\omega)$ by Fourier transforming $F_{ZZ}(k,t)$. In the $r_s = 0$ (OCP) limit, where the electrons form a uniform (nonpolarizable) background $S_{ZZ}(k,\omega)$ which there reduces to the dynamical structure factor of the bare ions, is simply the k-dependent spectrum of the ionic plasma oscillations [51]. In the long wavelength limit the mode is undamped, and its characteristic frequency is the ion plasma frequency ω_{pl}. Adiabatic electron polarization transforms this ionic plasmon (or optic) mode into an acoustic mode for any finite value of r_s [53,54]. This mode is to be identified with the familiar low-frequency ion-acoustic mode. Only if the system were treated as a fully dynamical ion-electron plasma, would the high-frequency plasma oscillation mode appear, which is related to the fast electronic motions. This mode is obviously
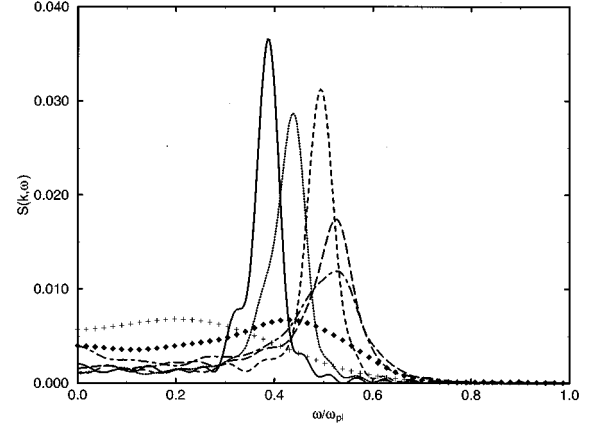

FIG. 14. Charge-charge dynamical structure factor at $r_s = 1$ for different values of momentum: $ka = 0.715$ (solid line), 1.011 (dotted), 1.238 (short-dashed), 1.599 (long-dashed), 2.022 (dot-dashed), 2.476 (diamonds), and 2.948 (crosses), from a simulation with 162 H atoms. The curves have been obtained by Fourier transforming the autocorrelation functions (8), filtering with an appropriate decaying exponential those corresponding to the largest wave vectors in order to reduce noise. All curves are normalized by the static structure factor $S_{ZZ}(k) = \int_0^\infty S_{ZZ}(k,\omega)d\omega$, such that the area under every curve is 1.

not accessible by adiabatic MD simulations. The conjectured scenario is confirmed by the results of our AIMD simulations. The dynamical structure factor $S_{ZZ}(k,\omega)$ was computed for the smallest wave number k compatible with the PBC ($ka = 1.031$ for the 54 atom system) and for selected larger wave numbers ($ka < 3$). The resulting $S_{ZZ}(k,\omega)$ for $r_s = 0.5$, $r_s = 1$, and $r_s = 1.2$ are shown in Fig. 13, for the smallest available wave number, and at a temperature just above melting. The sharp peaks are characteristic of the long-lived (weakly damped) mode anticipated above. The peaks shift to lower frequencies as r_s increases due to enhanced electron screening, and in accord with the behavior of
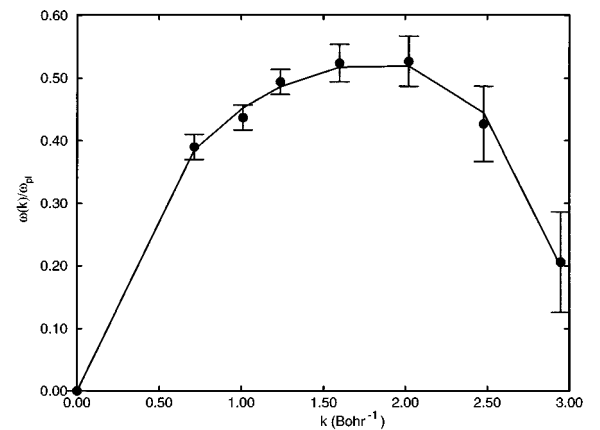

FIG. 15. Dispersion relation for the collective ion-acoustic mode in $S_{ZZ}(k,\omega)$, at $r_s = 1$. Filled circles are points corresponding to the k vectors allowed by the PBC, in a simulation box containing 162 H atoms. The solid line is a guide to the eye, arising from a 4th-degree polynomial fit to the data.
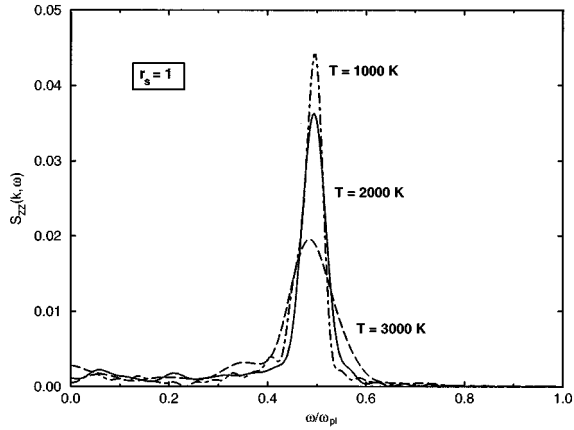
FIG. 16. Dynamical structure factor at $r_s = 1$ for $ka = 1.238$ at $T = 1000$ K (dot-dashed line), $T = 2000$ K (solid line), and $T = 3000$ K (dashed line).

the plasmonlike peak in the spectrum of the VACF (the single-particle excitation coupled to the collective plasmon mode). The k dependence of the spectrum $S_{ZZ}(k, \omega)$ is illustrated in Fig. 14, for $r_s = 1$; the resulting dispersion curve is shown in Fig. 15. A striking feature is the nearly constant width of the resonance peaks for $ka < 1.5$, pointing to a nearly k-independent damping mechanism. The damping increases dramatically at larger wave numbers, while the dispersion curve bends over; the behavior is reminiscent of that observed for a classical fluid of atoms interacting via an effective Yukawa potential [54]. The bending over may be regarded as a remnant of the negative dispersion of the plasmon mode observed in the strongly coupled OCP [51]. From the initial slope of the dispersion relation, we estimate a sound velocity of $c_s \approx 70$ km/s at $r_s = 1$, which is is consistent with the extrapolation of very recent results by Alavi, Parrinello, and Frenkel to the ultrahigh density regime [31]. Sound velocities are relevant to the determination of global free oscillations of Jovian planets, which have been recently measured for Jupiter [55].

The remarkable feature is that this collective mode is much sharper than the usual sound mode observed in metals at comparable wave numbers. Moreover, the peaks do not shift significantly with temperature, although they broaden. However, particularly for low values of k, the signature of the collective mode can be detectable up to quite high temperatures (well above 3000 K). This is seen in Fig. 16, where we plot the dynamical structure factor for $ka = 1.238$ (i.e., just before the bending-down point) in the 162-atom sample at $r_s = 1$ and for three different temperatures. It is interesting to note that this is precisely the temperature range where a transition is expected to occur to the molecular (H_2) fluid phase at lower densities [28]. The observed collective behavior may be regarded as characteristic of the metallic phase of hydrogen, and is expected to change dramatically at the transition towards the molecular phase, which begins to show up at low temperatures at $r_s \approx 1.3$. Therefore, an analysis of $S_{ZZ}(k, \omega)$ may provide an efficient diagnostic to locate the plasma phase transition at finite temperature.

IX. CONCLUSIONS

The main conclusions to be drawn from the present AIMD simulations of the hydrogen plasma in the high-density ($r_s \lesssim 1.2$) regime may be summarized as follows:

(a) Due to the significant spacing between the quantized electronic states in the vicinity of the Fermi surface, the N dependence of the statistical averages must be treated with great care, in order to extract meaningful results.

(b) A linear-response treatment of the ion-electron correlations yields reasonable results at $r_s = 0.5$, but becomes rapidly unreliable at lower densities.

(c) The bcc structure, which is the stable low-temperature solid phase at least up to $r_s = 0.5$, becomes unstable at lower densities, where hcp and simple-hexagonal phases appear. More work is needed to determine the full low-temperature phase diagram, also including zero-point-motion effects.

(d) The melting temperature drops sharply with decreasing density, due to the enhanced efficiency of electron screening of the effective interaction between ions. Interesting physics is likely to arise in the region of $r_s \approx 1.1$ and $T \approx 100 - 200$ K, where the existence of a bcc-hcp(fcc)-liquid triple point is argued, in a region where quantum effects in the protons are non-negligible.

(e) The fluid metallic phase behaves very much like a simple atomic liquid from a structural point of view, but the longitudinal collective dynamics of the ions retain a strong plasmalike character at intermediate wave numbers. This reflects itself in unusually sharp peaks in the charge-fluctuation spectrum, which are gradually shifted to lower frequencies with decreasing density, as a result of electron screening. The damping, however, appears to be surprisingly insensitive to density, but is significantly enhanced by temperature. The acoustic character of the longitudinal mode is recovered at sufficiently small wave numbers ($ka < 1$), in qualitative agreement with a simple linear screening picture. A strong damping of the mode at intermediate wave numbers should be a clear-cut signature of the plasma-to-molecular phase transition, which is expected to start at $T = 0$ around $r_s = 1.3$, and to move to finite temperatures of the order of a few thousand K at lower densities ($r_s > 1.3$) [28].

(f) The single-particle motion of the ions couples to the longitudinal collective mode, and reflects itself in a striking oscillatory behavior of the velocity autocorrelation function, which is reminiscent of the behavior of the OCP, despite the action of strong electron screening. The resulting ionic self-diffusion constant is strongly enhanced at lower densities, for identical values of the plasma coupling constant Γ, but follows a power law similar to that observed in the OCP. The present AIMD simulations will be extended to lower densities, in order to characterize the plasma-to-molecular phase transition, starting from the high density, metallic side.

 [1] E. Wigner and H. B. Huntington, J. Chem. Phys. **3**, 764 (1935); H. K. Mao and R. J. Hemley, Science **244**, 1462 (1989).

 [2] See, H. K. Mao and R. J. Hemley, Rev. Mod. Phys. **66**, 671 (1994), and references therein. See also I. F. Silvera, in *Simple Molecular Systems at Very High Pressure*, edited by A. Polian, P. Loubeyre, and N. Bocarra (Plenum, New York, 1989).

 [3] L. Cui, N. H. Chen, and I. F. Silvera, Phys. Rev. Lett. **74**, 4011 (1995).

 [4] A. Ruoff (private communication).

 [5] N. W. Ashcroft, Phys. World, July, 43 (1995).

 [6] M. Hanfland, R. J. Hemley, and H. K. Mao, Phys. Rev. Lett. **70**, 3760 (1993).

 [7] R. J. Hemley and H. K. Mao, Phys. Rev. Lett. **61**, 857 (1988).

 [8] E. Kaxiras, J. Broughton, and R. J. Hemley, Phys. Rev. Lett. **67**, 1138 (1991); E. Kaxiras and J. Broughton, Europhys. Lett. **17**, 151 (1992).

 [9] H. Chacham and S. G. Louie, Phys. Rev. Lett. **66**, 64 (1991).

[10] M. P. Surh, T. W. Barbee III, and C. Mailhiot, Phys. Rev. Lett. **70**, 4090 (1993).

[11] H. Nagara and T. Nakamura, Phys. Rev. Lett. **68**, 2468 (1992).

[12] J. S. Tse and D. D. Klug, Nature **378**, 595 (1995).

[13] I. I. Mazin and R. E. Cohen, Phys. Rev. B **52**, R8597 (1995).

[14] V. Natoli, R. M. Martin, and D. M. Ceperley, Phys. Rev. Lett. **70**, 1952 (1995).

[15] T. W. Barbee III, A. Garcia, M. L. Cohen, and J. L. Martins, Phys. Rev. Lett. **62**, 1150 (1989).

[16] T. W. Barbee III and M. L. Cohen, Phys. Rev. B **44**, 11 563 (1991).

[17] P. Focher, G. L. Chiarotti, M. Bernasconi, E. Tosatti, and M. Parrinello, Europhys. Lett. **36**, 345 (1994).

[18] J. Kohanoff, S. Scandolo, G. L. Chiarotti, and E. Tosatti (unpublished).

[19] D. M. Ceperley and B. J. Alder, Phys. Rev. B **36**, 2092 (1987).

[20] V. Natoli, R. M. Martin, and D. M. Ceperley, Phys. Rev. Lett. **70**, 1952 (1993).

[21] M. Baus and J.-P. Hansen, Phys. Rep. **59**, 1 (1980); S. Ichimaru, H. Iyetomi, and S. Tanaka, *ibid.* **149**, 91 (1987).

[22] D. M. Ceperley (private communication).

[23] D. Hohl, V. Natoli, D. M. Ceperley, and R. M. Martin, Phys. Rev. Lett. **71**, 541 (1993).

[24] J. Kohanoff and J.-P. Hansen, Phys. Rev. Lett. **74**, 626 (1995).

[25] A. Alavi, J. Kohanoff, M. Parrinello, and D. Frenkel, Phys. Rev. Lett. **73**, 2599 (1994).

[26] C. Pierleoni, D. M. Ceperley, B. Bernu, and W. R. Magro, Phys. Rev. Lett. **73**, 2145 (1994).

[27] J. Kohanoff, C. Pierleoni, and D. M. Ceperley (unpublished).

[28] W. J. Nellis, M. Ross, and N. C. Holmes, Science **269**, 1249 (1995); S. T. Weir, A. C. Mitchell, and W. J. Nellis, Phys. Rev. Lett. **76**, 1860 (1996).

[29] G. Chabrier, D. Saumon, W. B. Hubbard, and J. I. Lunine, Astrophys. J. **391**, 817 (1992), and references therein.

[30] W. R. Magro, D. M. Ceperley, C. Pierleoni, and B. Bernu, Phys. Rev. Lett **76**, 1240 (1996).

[31] A. Alavi, M. Parrinello, and D. Frenkel, Science **269**, 1252 (1995).

[32] D. Saumon, W. B. Hubbard, G. Chabrier, and H. M. van Horn, Astrophys. J. **391**, 827 (1992).

[33] R. Car and M. Parrinello, Phys. Rev. Lett. **55**, 2471 (1985); for a recent review, see, G. Galli and M. Parrinello in *Computer Simulations in Materials Science*, edited by M. Meyer and V. Pontikis (Kluwer, Dordrecht, 1991) p. 282.

[34] For a comprehensive treatise, see, e.g., R. G. Parr and W. Yang, *Density Functional Theory of Atoms and Molecules*, (Oxford University Press, New York, 1989).

[35] H. Xu, J.-P. Hansen, and D. Chandler, Europhys. Lett. **26**, 419 (1994).

[36] D. M. Ceperley and B. J. Alder, Phys. Rev. Lett. **45**, 566 (1980); D. M. Ceperley, Phys. Rev. B **18**, 3126 (1978).

[37] Z. Lin and J. Harris, J. Phys. Condens. Matter **4**, 1055 (1992).

[38] W. B. Hubbard and M. S. Marley, in *Strongly Coupled Plasma Physics*, Vol. 154 of *NATO Advanced Study Institute, Series B: Physics*, edited by F. J. Rogers and H. E. Dewitt (Plenum, New York, 1987).

[39] S. Galam and J.-P. Hansen, Phys. Rev. A **14**, 816 (1976).

[40] J. P. Perdew and A. Zunger, Phys. Rev. B **23**, 5048 (1981).

[41] F. Ercolessi and G. B. Adams, Europhys. Lett. **26**, 583 (1994).

[42] J. Hafner, *From Hamiltonians to Phase Diagrams*, Vol. 70 of *Springer Series in Solid-State Sciences* (Springer, Berlin, 1987).

[43] P. Blöchl and M. Parrinello, Phys. Rev. B **45**, 9413 (1992).

[44] T. A. Arias, M. C. Payne, and J. D. Joannopoulos, Phys. Rev. Lett. **69**, 1077 (1992).

[45] M. P. Grumbach, D. Hohl, R. M. Martin, and R. Car, J. Phys. Condens. Matter **6**, 1999 (1994).

[46] G. Pastore, E. Smargiassi, and F. Buda, Phys. Rev. A **44**, 6334 (1991).

[47] M. O. Robbins, K. Kremer, and G. S. Grest, J. Chem. Phys. **88**, 3286 (1988).

[48] M. W. C. Dharma-wardana and F. Perrot, Phys. Rev. A **26**, 2096 (1982).

[49] C. Pierleoni (private communication).

[50] A. Alavi (private communication).

[51] J. P. Hansen, I. R. McDonald, and E. L. Pollock, Phys. Rev. A **11**, 1025 (1975).

[52] G. Zérah, J. Clérouin, and E. L. Pollock, Phys. Rev. Lett. **69**, 446 (1992).

[53] F. Postogna and M. P. Tosi, Nuovo Cimento **B55**, 399 (1980).

[54] J. L. Barrat, J. P. Hansen, and H. Totsuji, J. Phys. C **21**, 4511 (1988).

[55] B. Mosser, D. Me'karnia, J. P. Maillard, J. Gay, D. Gautier, and P. Delache, Astron. Astrophys. **267**, 604 (1993).